Journal of Materials Chemistry A

Accepted Manuscript

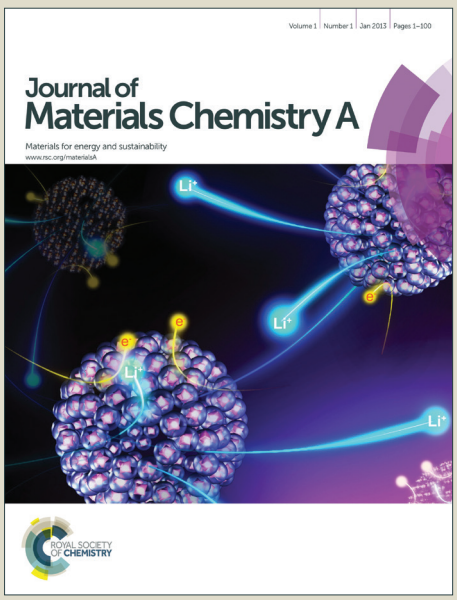

ROYAL SOCIETY OF CHEMISTRY

www.rsc.org/materialsA

Metal and F dual-doping to synchronously improve electronic transport rate and lifetime for TiO_2 photoanode to enhance dye-sensitized solar cells performances

Yandong Duan,‡[ab] Jiaxin Zheng,‡[a] Ming Xu,[a] Xiaohe Song,[a] Nianqing Fu,[bc] Yanyan Fang,[b] Xiaowen Zhou,[b] Yuan Lin*[ab] and Feng Pan*[a]

[a]School of Advanced Materials, Peking University Shenzhen Graduate School, Shenzhen 518055, China

[b]Beijing National Laboratory for Molecular Sciences, Key Laboratory of Photochemistry, Institute of Chemistry, Chinese Academy of Sciences, Beijing 100190, China

[c]Department of Applied Physics, The Hong Kong Polytechnic University, Hung Hom, Kowloon, Hong Kong, China

† Electronic supplementary information (ESI) available. See DOI:

‡ Y. D. Duan and J. X. Zheng contributed equally to this work.

*Corresponding author: linyuan@iccas.ac.cnTel: 86-10-82615031 Fax: 86-10-82617315

*Corresponding author: panfeng@pkusz.edu.cnTel: 86-755-26033200

Abstract: A general strategy to synchronously improve electronic transport rate and lifetime for TiO_2 photoanode by metal and F^- dual dopingare proposed and demonstrated for dye-sensitized solar cells (DSSCs) for the first time. Tin and fluorine dual-doped TiO_2 nanoparticles are prepared and X-ray photoelectron spectroscopy (XPS) analysis indicates that the Sn atoms and the F atoms mainly locate in the TiO_2 lattice and on the TiO_2 particles surface, respectively. The DSSC based on Sn/F-TiO_2 sample shows a high photoconversion efficiency of 8.89 % under an AM 1.5 solar condition (100mW cm^{-2}), higher than those for the undoped TiO_2 nanoparticles (7.12 %) and the solely Sn (8.14 %) or F doped (8.31 %) samples. This improvement is attributed to the combined effects of a faster electron transport rate and a longer electron lifetime in the dual-doped TiO_2 film. Following this strategy, we also prepare Ta/F, Nb/F, and Sb/F dual-doped TiO_2 nanoparticles and find that the performance of DSSCs based on all the dual-doped samples is further improved compared with the single doping cases. Finally, through density functional theory (DFT) calculations, the mechanism behind the improvement by tin and fluorine dual-doping is discussed in detail.

Keywords: dye-sensitized solar cell, anatase, metal-doping, electron recombination, fluorine-doping

Introduction

Due to their low cost production, environmentally-friendly, and relatively high photoelectric conversion efficiency (PCE), dye-sensitized solar cells (DSSCs) have attracted much attention in recent years. A typical DSSC consists of a dye-sensitized electrode (photoanode), a redox electrolyte, and a platinized counter electrode.[1] Among all kinds of photoanode materials (TiO_2, SnO_2, ZnO, Nb_2O_5, $SrTiO_3$, and Zn_2SnO_4), the mesoscopic anatase TiO_2 film is most widely studied due to its wide band-gap and high dye adsorption, and the PCE of DSSCs based anatase TiO_2 reaches higher than 13 %.[2] The mesoscopic TiO_2 film plays a critical role in the performance of DSSCs in light energy conversion, including the electron transfer from the dye molecules to the conduction band of TiO_2 and the electron transport to the external circuit. Therefore, rational design of the mesoscopic TiO_2 film is crucial to improve the overall power conversion efficiency of devices.

To improve the performance of TiO_2 photoanode, much work has been focused on enhancing the charge collection efficiency, such as tuning the position of conduction band, improving the charge transport,[1] and suppressing the charge recombination.[3-7] Doping TiO_2 with metal ions is a commonly adopted method to tailor the properties of TiO_2 photoanode,[8] such as to improve the charge transport properties.[9-12] Table 1 shows the reported high values of PCE obtained in the DSSCs based on different doped TiO_2 photoanodes (Table S1 presents the more detailed summary for the photovoltaic performance of the DSSCs based on different doped TiO_2, SnO_2, and ZnO composites photoanodes). Recently it is shown that homovalent doping (Zr doping) would also increase electron density and uplift Fermi level of TiO_2 thereby increasing the performance of DSSCs.[36] Titanium and tin have the same number of valence electrons, and there is a large difference of ionic radii between them (r_{SnIV}=0.69Å, r_{TiIV}=0.61Å), similar to that between Zr and Ti. Their outer layer valence electrons also occupy different orbitals ($5s^2$ and $5p^2$ for Sn, and 3d for Ti). Our previous work also found

that an increasing electron density could be achieved by homovalent substitution of Sn doping in TiO_2, which offered lower transport resistance. [37]

However, metal ion doping also introduces more charge recombination centers and leads to increased charge recombination rate. Therefore, how to suppress the electron recombination to further improve the performance of metal-doped TiO_2 DSSCs becomes a challenging and extensively studied topic. Recently, several work reported that fluorine doping could inhibit the charge recombination by tightly holding trapped electrons due to the strong electronegativity of fuorine and formation of electron trapping sites.[29, 34, 35] Based on these results, we proposed that the performance of metal-doped TiO_2 DSSCs could be further improved by combining with F doping to inhibit the charge recombination.

In this work, Sn and F dual-doped TiO_2 was synthesized via a simple hydrothermal method, and the performance of DSSCs based on Sn and F dual-doped TiO_2 was studied. We found that the charge transport of TiO_2 is improved and the charge recombination is suppressed in the dual-doped TiO_2 films. Thus, compared with DSSCs based on solely Sn-doped (8.14%) TiO_2 films, DSSCs based on Sn and F dual-doped TiO_2 exhibit a higher PCE (8.89%) under an AM 1.5 solar condition (100 mW cm^{-2}), which is also a high PCE compared with other reported high values for TiO_2 DSSCs (Table 1). Furthermore, we also studied the performance of DSSCs based on Ta/F, Nb/F, and Sb/F dual-doped TiO_2, and found that the performance of DSSCs based on the above dual-doped TiO_2 simples were further improved compared with those of DSSCs based on solely doped TiO_2. Finally, the dual doping effect is studied by density functional theory (DFT) calculations.

Results and discussion

The XRD patterns of the synthesized samples are presented in Fig. 1. All peaks of the samples can be indexed to the anatase phase (JCPDS No. 89-4921), indicating that the anatase nanocrystalline structure is retained after doping. The lattice parameters for TiO_2 and the doped TiO_2 were estimated from the positions of the main diffraction peaks of the tetragonal

phase. The strongest diffraction peak (101) for the anatase phase, located at 25.36°, was studied and used in the determination of the average crystalline size of the samples using the Scherrer equation. As shown in Table 2, the crystallite size was calculated to be ca. 14 nm for both TiO_2 and the doped TiO_2 samples. Table 2 shows the average values of the unit cell parameters for pure TiO_2 and the doped TiO_2 samples calculated by Bragg's formula. It can be seen from Table 2that the insertion of Sn^{4+} into the TiO_2 lattice could induce a slight expansion of the lattice, which could be attributed to the larger effect ionic radius of the Sn^{4+} ionic (0.069 nm) than that of Ti^{4+}(0.061 nm). The TiO_2 lattice has little change after doping with F, which was ascribed to the fact that F atoms exist mainly on the TiO_2 particles surface (from XPS results). Therefore, the TiO_2-Sn sample and TiO_2-Sn/F have similar lattice parameters.

Fig. 2 presents the TEM images of TiO_2, TiO_2-Sn, TiO_2-F, and TiO_2-Sn/F nanoparticles. It can be clearly seen that the average diameter size of TiO_2 and the doped TiO_2 samples is ca. 14 nm, which is in good agreement with the average size calculated from XRD results. The HRTEM images in the inset of Fig. 2 indicate the high crystallinity of the TiO_2 and the doped TiO_2 nanoparticles.

To investigate the chemical states of doping Sn and F ions in TiO_2, the binding energy (BE) of Ti_{2p}, Sn_{3d}, and F_{1s} for the samples have been studied by XPS. Fig. 3(a) shows the Ti_{2p} XPS spectra of TiO_2, TiO_2-Sn and TiO_2-Sn/F. Comparing with the spectra for pure TiO_2, the two peaks of the Ti_{2p} spectra for TiO_2-Sn exhibit a positive shift, which is ascribed to the interaction between tin atoms, oxygen atoms and titanium atoms. Consistent with this result, the Sn_{3d} spectra for TiO_2-Sn sample reveal a negative shift (ca. 0.2 eV) toward lower binding energy compared to that of SnO_2(Fig. 3b), indicating the variation in electron negativities of the Ti and Sn elements (Ti = 1.54, Sn = 1.96).[37] Compared with the TiO_2-Sn (458.7 and 463.4 eV for $Ti_{2p3/2}$ and $Ti_{2p1/2}$), the binding energy of TiO_2-Sn/F increased to 458.9 and 463.6 eV after F-doping (TiF_4) (as shown in Fig. 3(a)). This can be attributed to the different electron

negativity of fluorine compared to oxygen (F = 4.0, O = 3.44). Based on this effect, the Sn_{3d} spectra for TiO_2-Sn/F sample reveal a positive shift (ca. 0.2 eV) toward lower binding energy compared to that of TiO_2-Sn. Fig. 3(c) gives the high-resolution XPS spectrum of F_{1s} (ca. 684.6 eV). A small peak are identified at higher energies (689.2 eV), which is ascribed to the lattice F. Therefore, the detected F should mainly correspond to either graft on the TiO_2 surface by substitution of the hydroxyl groups or physical adsorption.[29]

The flatband potentials of TiO_2 and the doped TiO_2 films at the semiconductor/electrolyte junction were obtained from Mott-Schottky plots (taken in the dark) using the following equation:[38]

$$\frac{1}{C^2} = \frac{2}{A^2 \varepsilon_{TiO_2} \cdot \varepsilon_0 \cdot e_0 \cdot N_D}(E - E_{FB} - \frac{kT}{e_0}) \quad (39)$$

(where C being the capacitance of the space charge region, ε_0 the vacuum permittivity, ε_{TiO_2} the dielectric constant of the TiO_2 layer, e_0 the elementary charge, E the applied potential, E_{fb} the flat band potential, k the Boltzmann constant, T the absolute temperature, N_D the donor density, and A the active surface). The intercept of the fitted lines are E_{fb} and the values are shown in Fig.4. The slope of the fitted lines are used to calculate the donor density (Table S2). Though the E_{fb} of TiO_2 exhibits a slight positive shift after doping with F. The E_{fb} of TiO_2 was negatively shifted after doping with Sn/F, indicating a shift away from the redox potential, thereby an increment of V_{oc}.

Fig. 5 shows the j-V plots of the DSSCs based on the TiO_2 and the doped TiO_2 photoanodes under light intensity of 100 mW cm^{-2} at AM1.5. The photovoltaic parameters are listed in Table 3. j_{sc}, V_{oc} and FF are short circuit photocurrent, open circuit photovoltage, and fill factor, respectively. For DSSCs based on pure TiO_2, j_{sc}, V_{oc}, FF, and η are 14.82 mA cm^{-2}, 686 mV, 0.71, and 7.22%, respectively. After tin doping, the short-circuit photocurrent density, the open-circuit voltage and the photoelectric conversion efficiency of DSSCs were enhanced. The dye loading amount shown in Table 3 is similar for all the films, indicating

that the enhancement of photocurrent for the doped TiO_2 is not due to the increase of the dye adsorption. The higher j_{sc} results from the enhanced electron transport (due to the changes in the electron density, Table S2) in the TiO_2 films and the higher V_{oc} should result from the elevated E_{fb}.[37] The performance of DSSCs was further increased after doping with F. This result could be ascribed to the longer electron lifetime in the TiO_2 films after introducing fluorine ion. And the longer electron lifetime could be explained in the IMVS part. The F-doped TiO_2 (TiF_4 as a doping source) was used as reference to further confirm the effect of fluorine ion. Based on these results, we further studied the performance of DSSCs after Ta/F, Nb/F, and Sb/F doping and the results are shown in Fig. S1 and Table S2**.** We found that the performance of DSSCs based on Ta/F, Nb/F and Sb/F dual-doped TiO_2 is much higher than that of DSSCs based on Ta, Nb and Sb solely doped TiO_2.

To better understand the dynamics of electron transport/recombination in the titania films, the EIS measurements were performed over the frequency range of 0.1 Hz to 100 kHz under an AM 1.5 solar condition (100 mW cm^{-2}). The applied bias voltage was set to the open-circuit voltage (V_{oc}) of the DSSCs, and an AC amplitude of 5 mV was applied. Fig. 6 shows the Nyquist plots under the open-circuit condition for the DSSCs. All spectra in Fig. 6 can be described by two typical semicircles observed in the measured frequency at photoelectrodes, which are attributed to the electrochemical reaction at the Pt counter electrode, charge transfer and recombination at the TiO_2/dye/electrolyte interface. The semicircles in the Nyquist plots corresponding to a middle-frequency area (in the 10-100 Hz range) areattributed to the electron transfer and recombination at the TiO_2/dye/electrolyte interface. The impedance spectra were fit to a transmission line model equivalent circuit, as presented in the Fig. S2. [40-43] The fitting results shown in Table 4 indicates that the electron transport resistance R_w decreases after Sn doping. Although the R_w increases after doping with F, the electron transport performance is still improved by dual-doping with Sn and F. The interfacial charge

recombination resistance R_k of the F-doping cell is larger than that without F-doping, indicating a lower recombination rate than that of the sample with no F-doping.

To further confirm the synergistic effects of Sn/F dual-doping on electron transport in the TiO_2 film and electron recombination between the injected electron and the redox electrolyte (I_3^-), we carried out IMPS/IMVS measurements. Intensity modulation photocurrent spectroscopy (IMPS) is employed to analyze the dynamic of electron transport in the TiO_2 and the doped TiO_2, and the results are shown in Fig.7(a). The electron transport time (τ_d) for the pure TiO_2, TiO_2-Sn, TiO_2-F, TiO_2-Sn/F are 8.3, 5.4, 9, and 5.9 ms, respectively. The shorter transport time of the TiO_2 and TiO_2-Sn/F based films means faster electron transport rate, which is favorable to the improvement of charge-collection efficiency and photocurrent density. The IMVS shows that the lifetime or recombination time (τ_n) of the TiO_2-Sn/F based cell is larger than that of the TiO_2-Sn(Fig.7(b)), in agreement with the results of EIS measurement. The charge collection efficiency (η_{cc}) was introduced to quantitative analyze the effect of electron lifetime and transport time. η_{cc} can be calculated according to the equation: $\eta_{cc}=1-(\tau_d/\tau_n)$. The obtained η_{cc} value for TiO_2, TiO_2-Sn, TiO_2-F, and TiO_2-Sn/F electrodes are 85.6, 89.1, 90.0, and 93.9%, respectively. This result is in accordance with the tendency of short-circuit photocurrent density variation.

In order to identify the effect of Ti atoms partially substituted by the Sn atoms to the electronic conductance of $Ti_{1-x}Sn_xO_2$, we performed a density functional theory (DFT) study of the density of states (DOS) for our materials. The calculated band gap of TiO_2 is 2.07 eV, which is lower than the experimental value of 3.2 eV.[44] It is well known that the GGA method underestimates the band gap, especially for the system with strong correlations or weak Coulomb screening. The band gap can be corrected to be 3.03 eV if the hybrid functional due to Heyd, Scuseria, and Ernzerhof (HSE06) with screening parameter of 0.2 is employed,[45] which is nearly the same value as the experimental value. The band gap can also be corrected by the scissors operator to match with the experimental value. However, even though the

correction is not made, the GGA results can still predict the trend of variation for the band gap and the Fermi level shift under different doping concentration.

For each *x* value, we have considered at least four substitution structures and found that there is little difference among them. Fig.8 shows the doping model and the DOS for $Ti_{1-x}Sn_xO_2$ with different substitution degrees. Our calculation revealed that, after Ti substituted by Sn, the valence band maximum (VBM) remains almost unchanged and the conductance band minimum (CBM) shifts upward a little by 0.06 eV. Thus, the band gap is enlarged by 0.03~0.08 eV when the Ti atoms are substituted by the Sn atoms, consistent with previous theoretical and experimental results,[46,47] which also accounts for our experimental observation that the conductance band shifts upward after Sn doping and increased V_{OC} was obtained. The band gap enlargement is attributed to the appearance of the Sn_{5s} and Sn_{5p} orbitals in the CBM (the VBM is mainly composed of O_{2p} states, and the CBM is mainly composed of Ti_{3d} states). However, the doping level needs to be restricted as the increased lattice strain after Sn-doping would contribute to charge recombination, and a trade-off between doping concentration and photovoltaic properties is needed.[36]

The electronic structures of clean and F-adsorbed surfaces are also calculated, as shown in Fig.9. From the most energy stable adsorbtion structure, we can see that the F atoms are bonded with the surface fivefold Ti. The bond length is 1.9 Å, and the binding energy is 1.0 eV, indicating a strong chemisorption. Compared with the clean surfaces of TiO_2, the Fermi levels for (101) and (001) surfaces adsorbed with F atoms is shifted toward the valence band by 0.5 and 1.1 eV, respectively. Meanwhile, the band gaps are also enlarged by 0.14 eV and 0.3 eV, respectively. Combing the projected DOS (PDOS) and partial DOS, we can see that for clean TiO_2 surface, the valence band and conductance band near the Fermi level are mainly composed of O_{2p} and Ti_{3d} orbitals, respectively. After the chemisorption of F atoms on the surface, the F_{2p} orbitals also contribute to the valence band near the Fermi level (blue line in Fig. 9), and the stronger bond of Ti-F than the Ti-O will lower the energy of the electrons

of the valence band, thus leading to the downward shift of the Fermi level and the enlarged band gap. As a result, the F adsorbtion will produce charge trapping sites on the surface and suppress the charge recombination at the interface by holding trapped electrons, thus leading to the longer electron lifetime as observed in the IMVS measurements.

Conclusions

A general dual-doping strategy was developed for TiO_2 based dye-sensitized solar cells performances.Tin and fluorine dual-doped TiO_2 nanoparticles were successfully prepared by hydrothermal method. DSSCs based on Sn/F dual-doped TiO_2 exhibit higher PCE (8.89%) than those for the undoped TiO_2 nanoparticles and the solely Sn or F doped samples, which is attributed to the combined effect of a faster electron transportation and the longer electron lifetime in the dual-doped TiO_2 film. This combined effect of dual-doing is also demonstrated to be effective for DSSCs based on Ta/F, Nb/F, and Sb/F dual-doped TiO_2, and the performance of DSSCs based on such dual-doped TiO_2 samples is higher than that of DSSCs based on solely doped TiO_2. By employing the DFT calculations, the mechanism behind the improvement by tin and fluorine dual-doping is discussed in detail. This work may open a new way to further improve the performance of DSSCs by metal/F dual-doping method, promoting the progress of DSSCs toward commercial applications.

Experimental section

Materials

Tetrabutyl titanate (98%, Sinopharm Chemical Reagent Co., Ltd), tin(IV) tert-butoxide ($Sn(OC_4H_9)_4$, 99.9%, Alfa),Titanium(IV) fluoride (98%, Alfa), butanol (Beijing Chemical Works), acetic acid (Beijing Chemical Works), 3-methoxypropionitrile (MPN, 99 %, GC, Alfa), LiI (AR, Acros), I_2 (AR, Acros), and 4-*tert*-butylpyridine (TBP, AR, Aldrich), were commercially available and used without further purification. 3-Hexyl-1-methylimidazolium Iodide (HMII) was prepared according to the literature.[48]

Synthesis of TiO_2 and the doped TiO_2 nanoparticles

Both TiO_2 and the doped TiO_2 were synthesized by using the hydrothermal method. Tetrabutyl titanate (5 mL), butanol (30 mL), acetone (5 mL), and acetic acid (5 mL) were mixed. A mixture of butanol (20 mL) and distilled water (1.5 mL) was then added to the above solution. After being stirred continuously for 0.5 h, the mixture was transferred into an autoclave for the hydrothermal process at 240 ℃ for 6 h. After being cooled to room temperature, the concentrated colloid contained 10-13wt% TiO_2 was obtained by rotary evaporation. For preparing Sn-doped, F-doped and the Sn/F dual-doped samples, $Sn(OC_4H_9)_4$, TiF_4 and $Sn(OC_4H_9)_4/TiF_4$ were added to the tetrabutyl titanate, respectively. The optimized Sn doping amount was chosen according to the literature.[37] Molar ratio of $Sn(OC_4H_9)_4$ and $Ti(OC_4H_9)_4$ in all the samples was 0.5:100. The optimized molar ratio of TiF_4 and $Ti(OC_4H_9)_4$ of the F-doped TiO_2 and Sn/F doped samples was 0.75:100.

Cell fabrication and photovoltaic measurements

TiO_2 and the doped TiO_2 films (ca. 11 μm) were fabricated on the FTO substrates (fluorine-doped SnO_2, 7 Ω/sq) using a doctor-blade method and the electrodes were heated at 450 °C for 30 min. After sintering, the electrodes were immersed in a dye bath containing *cis*-$Ru(H_2dcbpy)_2(NCS)_2$ (H_2dcbpy= 4,4'-dicarboxy-2,2'-bipyridyl) (N3) (0.5 mM) in ethanol for 24 h when the temperature cooled to about 80 ℃. The film thickness was obtained by CCD laser displacement sensor (Keyence corporation). The redox electrolyte was a mixture of LiI (0.5 M), I_2 (0.05 M), TBP (0.6 M) and HMII (0.6 M) in MPN. The counter electrode was Pt-coated FTO.

The photocurrent density-voltage (*j-V*) measurement was tested using a Keithley 2611 Source Meter (Keithley Instruments, Inc.). The light source was an AM 1.5 solar simulator (91160A, Newport Co.). The incident light intensity was 100 mW cm^{-2} calibrated with a

standard Si solar cell. The photoanode area of the DSSCs is 1 cm^2. The tested solar cells were masked to a working area of 0.2 cm^2.

Characterization

The crystal phase of the samples was analyzed by X-ray diffraction with Cu Kα radiation (XRD, D/MAX-2500, Rigaku Co., Japan). The accelerating voltage and the applied current were 40 kV and 150 mA, respectively. X-ray photoelectron spectroscopy (XPS) was used to measure the surface elements and the chemical state. The shift of the binding energy due to relative surface charging was corrected using the C_{1s} level at 284.8 eV as an internal standard. Transmission electron microscope (TEM) and high-resolution electron microscope (HRTEM) images were measured on a Tecnai G2 F20 U-TWIN transmission electron microscope operated at 200 kV.

Mott-Schottky analysis was performed in a three-electrode cell in the dark. TiO_2 or the doped TiO_2 single films without dyes (ca. 3 μm) were used as the electrode, a saturated calomel electrode (SCE) served as the reference electrode, and platinum wire was used as the counter electrode. The active area was 0.25 cm^2. TiO_2 and doped TiO_2 films (ca. 3 μm) adsorbed by dyes were used for the IMPS and IMVS test. IMPS and IMVS were performed using a green light emitting diode (max = 520 nm) driven by a solartron 1255B frequency-response analyzer. The LED provided both the dc and ac components of the illumination. Electrochemical impedance spectroscopy (EIS) data were obtained under 100 mW cm^{-2} illuminations, using a perturbation of ±10 mV over the open-circuit potential by using Solartron 1255B frequency analyzer and Solartron SI 1287 electrochemical interface system.

Calculation details

In order to model the TiO_2 doped by Sn, a 4×2×2, 4×4×2,4×3×2, 4×2×2 supercell based on the unit cell was constructed, allowing us to investigate different substitution degrees of $Ti_{1-x}Sn_xO_2$, with x=0, x=0.005, x=0.01, x=0.015, respectively, as shown in Fig.8. To study the F atoms adsorbtion on the TiO_2 particles surface, the slab technique is adopted to simulate the

TiO_2 particles surface. Both the (101) and (001) surfaces are considered here, which are the thermodynamically stable facet (more than 90%) and the much more reactive facet, respectively. In each case, stoichiometric 2×2 slabs are builded: the slab for clear (101) surface consists of 18 atomic layers and a total of 72 atoms, and the slab for clear (001) surface consists of 12 atomic layers and a total of 72 atoms. Because the exposed dangling bonds for each Ti and O atom of the surface can passivate each other, there is no need to consider the surface reconstruction to satisfy the electron counting rule. A vacuum butter space of at least 15 Å is set for slabs with adsorbed atoms. All atoms are relaxed without any constraint.

All calculations are performed using the plane-wave projector-augmented wave method[49, 50] as implemented in the Vienna ab initio simulation package.[51,52] The Perdew-Burke-Ernzerhof (PBE)[53] form of generalized gradient approximation (GGA) is chosen as the exchange-correlation potential. To obtain reliable optimized structures, the maximum residual force is less than 0.01 eV/Å and energies are converged to within 5×10^{-6} eV per atom, and the k-point mesh is set to 5×5×1 for F atoms adsorbtion. The k-point mesh of TiO_2 doped by Sn is set to 4×4×4, 3×3×3, 3×3×3, 4×4×4 with x=0, x=0.005, x =0.01, x =0.015, respectively, to calculate electronic properties. An energy cut-off of 520 eV was used in all cases.

Acknowledgements

This research was supported by Shenzhen Science and Technology Research Grant (No. ZDSY20130331145131323, JCYJ20120614150201123, SGLH20120928095706623 and JCYJ20120614150338154), National Natural Science Foundation of China (Grant No. 51303186), and National Research Fund for Fundamental Key Project (2012CB932903). Additionally, we acknowledge the support of ShenZhen National Super Computing Center.

Notes and references

†Electronic Supplementary Information (ESI) available: The performance of TiO_2 DSSCs after Ta/F, Nb/F, and Sb/F doping; Calculated total and partial density of states (DOS) for surfaces of anatase; Photovoltaic performance of the DSSCs based on TiO_2, SnO_2, and ZnO materials.

1. B. C. O'Regan and J. R. Durrant, *Acc. Chem. Res.*, 2009, **42**, 1799-1808.
2. A. Yella, H.W. Lee, H. N. Tsao, C. Yi, A. K. Chandiran, M. K. Nazeeruddin, E. W.G. Diau, C.Y. Yeh, S. M. Zakeeruddin and M. Grätzel, *Science*, 2011, **334**, 629-634.
3. J. H. Park, J. H. Noh, B. S. Han, S. S. Shin, I. J. Park, D. H. Kim and K. S. Hong, *J. Nanosci.Nanotech.*, 2012, **12**, 5091-5095.
4. R. Ghosh, Y. Hara, L. Aibabaei, K. Hanson, S. Rangan, R. Bartynski, T. J. Meyer and R. Lopez, *ACS Appl. Mater. Inter.*, 2012, **4**, 4566-4570.
5. Y. Zhang, L. L. Wang, B. K. Liu, J. L. Zhai, H. M. Fan, D. J. Wang, Y. H. Lin and T. F. Xie, *Electrochim.Acta*, 2011, **56**, 6517-6523.
6. X. Zhang, F. Liu, Q.L. Huang, G. Zhou and Z.S. Wang, *J. Phys. Chem. C*, 2011, **115**, 12665-12671.
7. G. Zhu, Z. Cheng, T. Lv, L. Pan, Q. Zhao and Z. Sun, *Nanoscale*, 2010, **2**, 1229-1232.
8. R. L. Z. Hoye, K. P. Musselman and J. L. MacManus-Driscoll, *APL Mater.*, 2013, **1**, 060701.
9. M. Wang, S. L. Bai, A. F. Chen, Y. D. Duan, Q. P. Liu, D. Q. Li and Y. Lin, *Electrochim. Acta*, 2012, **77**, 54-59.
10. C.N. Zhang, S. Chen, L. e. Mo, Y. Huang, H. Tian, L. Hu, Z. Huo, F. Kong, S. Dai and X. Pan, *J. Phys. Chem. C*, 2011,**115**, 16418-16424.
11. X. Lü, X. Mou, J. Wu, D. Zhang, L. Zhang, F. Huang, F. Xu and S. Huang, *Adv. Funct. Mater.*, 2010, **20**, 509-515.
12. K.P. Wang and H. Teng, *Phys. Chem. Chem. Phys.*, 2009, **11**, 9489-9496.
13. P. S. Archana, A. Gupta, M. M. Yusoff and R. Jose, *Phys. Chem. Chem. Phys.*, 2014, **16**, 7448-7454.
14. A. H. G. Niaki, A. M. Bakhshayesh and M. R. Mohammadi, *Sol. Energy*, 2014, **103**, 210-222.
15. Q. Liu, *Electrochim. Acta*, 2014, **129**, 459-462.
16. H. Seo, Y. Wang, D. Ichida, G. Uchida, N. Itagaki, K. Koga, M. Shiratani, S.-H. Nam and J.-H. Boo, *Jpn. J. Appl. Phys.*, 2013, **52**. 11NM02.
17. J. Zhang, W. Q. Peng, Z. H. Chen, H. Chen and L. Y. Han, *J. Phys. Chem. C*, 2012, **116**, 19182-19190.
18. S. G. So, K. Lee and P. Schmuki, *Phys. Status Solidi-R*, 2012, **6**, 169-171.
19. E. M. Jin, X. G. Zhao, J. Y. Park and H. B. Gu, *Nanoscale Res. Lett.*, 2012, **7**.

20. A. K. Chandiran, F. d. r. Sauvage, M. Casas-Cabanas, P. Comte, S. M. Zakeeruddin and M. Graetzel, *J. Phys. Chem. C*, 2010, **114**, 15849-15856.
21. J.H. Huang, P. Y. Hung, S.F. Hu and R.S. Liu, *J. Mater. Chem.*, 2010, **20**, 6505-6511.
22. T. R. C. K. Wijayarathna, G. M. L. P. Aponsu, Y. P. Y. P. Ariyasinghe, E. V. A. Premalal, G. K. R. Kumara and K. Tennakone, *Nanotechnology*, 2008, **19**, 485703.
23. C. Kim, K.S. Kim, H. Y. Kim and Y. S. Han, *J. Mater. Chem.*, 2008, **18**, 5809-5814.
24. M. Dürr, S. Rosselli, A. Yasuda and G. Nelles, *J. Phys. Chem. B*, 2006, **110**, 21899-21902.
25. P. S. Archana, E. Naveen Kumar, C. Vijila, S. Ramakrishna, M. M. Yusoff and R. Jose, *Dalton T*, 2013, **42**, 1024-1032.
26. A. Subramanian, J. S. Bow and H. W. Wang, *Thin Solid Films*, 2012, **520**, 7011-7017.
27. A. Subramanian and H. W. Wang, *Appl. Surf. Sci.*, 2012, **258**, 6479-6484.
28. Q. Sun, J. Zhang, P. Q. Wang, J. Zheng, X. N. Zhang, Y. Z. Cui, J. W. Feng and Y. J. Zhu, *J. Renew Sustain Energy*, 2012, **4**. 023104.
29. L. Song, H. Bin Yang, X. Wang, S. Y. Khoo, C. C. Wong, X. W. Liu and C. M. Li, *ACS Appl. Mater. Inter.*, 2012, **4**, 3712-3717.
30. Q. Q. Hou, Y. Z. Zheng, J. F. Chen, W. L. Zhou, J. Deng and X. Tao, *J. Mater. Chem.*, 2011, **21**, 3877-3883.
31. W. Guo, Y. Shen, G. Boschloo, A. Hagfeldt and T. Ma, *Electrochim. Acta*, 2011, **56**, 4611-4617.
32. J.Y. Park, K.H. Lee, B.S. Kim, C.S. Kim, S.E. Lee, K. Okuyama, H.D. Jang and T.O. Kim, *Rsc Adv.*, 2014, **4**, 9946-9952.
33. J. Yu, Y. Yang, R. Fan, L. Li and X. Li, *J. Phys. Chem. C*, 2014, **118**, 8795-8802.
34. H. Park and W. Choi, *J. Phys. Chem. B*, 2004, **108**, 4086-4093.
35. M. Samadpour, P. P. Boix, S. Gimenez, A. I. Zad, N. Taghavinia, I. Mora-Sero and J. Bisquert, *J. Phys. Chem. C*, 2011, **115**, 14400-14407.
36. P. S. Archana, A. Gupta, M. M. Yusoff and R. Jose, *Appl. Phys. Lett.*, 2014, **105**, 153901.
37. Y. Duan, N. Fu, Q. Liu, Y. Fang, X. Zhou, J. Zhang and Y. Lin, *J. Phys. Chem. C*, 2012, **116**, 8888-8893.
38. C. Baumanis and D. W. Bahnemann, *J. Phys. Chem. C*, 2008, **112**, 19097-19101.
39. Y. Furubayashi, T. Hitosugi and Y. Yamamoto1, *Appl. Phys. Lett.* 2005, **86**, 252101.
40. N.Q. Fu, Y.D. Duan, Y.Y. Fang, X.W. Zhou, X.R. Xiao and Y. Lin, *Electrochem. Commun.*, 2013, **34**, 254-257.
41. M. Adachi, M. Sakamoto, J. Jiu, Y. Ogata and S. Isoda, *J. Phys. Chem.B*, 2006, 110, 13872-13880.
42. J. Bisquert, *Phys. Chem. Chem.Phys.*, 2000, **2**, 4185-4192.
43. N. Fu, Y. Duan, Y. Fang, X. Zhou, Y. Liu, F. Peng, Y. Lin and H. Huang, *J. Power Sources*, 2014, **271**, 8-15.
44. W.J. Yin, S. Chen, J.H. Yang, X.G. Gong, Y. Yan and S.H. Wei, *Appl. Phys. Lett.*, 2010, **96**, 221901.
45. T. S. Bjørheim, A. Kuwabara and T. Norby, *J. Phys. Chem. C*, 2013, **117**, 5919-5930.

46. J. Li and H. C. Zeng, *J. Am. Chem. Soc.*, 2007, **129**, 15839-15847.
47. R. Long, Y. Dai, G. Meng and B. Huang, *Phys. Chem. Chem. Phys.*, 2009, **11**, 8165-8172.
48. P. Bonhôte, A.P. Dias, N. Papageorgiou, K. Kalyanasundaram and M. Grätzel, *Inorg. Chem.*, 1996, **35**, 1168-1178.
49. P. E. Blöchl, *Phys. Rev. B*, 1994, **50**, 17953-17979.
50. G. Kresse and D. Joubert, *Phys. Rev. B*, 1999, **59**, 1758.
51. G. Kresse and J. Furthmüller, *Phys. Rev. B*, 1996, **54**, 11169-11186.
52. G. Kresse and J. Furthmüller, *Comput. Mater. Sci.*, 1996, **6**, 15-50.
53. J. P. Perdew, K. Burke and M. Ernzerhof, *Phys. Rev. Lett.*, 1996, **77**, 3865-3868.

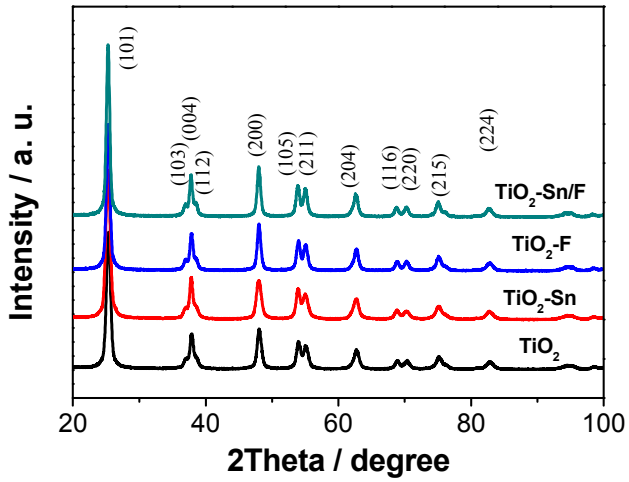

Fig. 1 XRD patterns of TiO_2, TiO_2-Sn, TiO_2-F and the TiO_2-Sn/F samples.

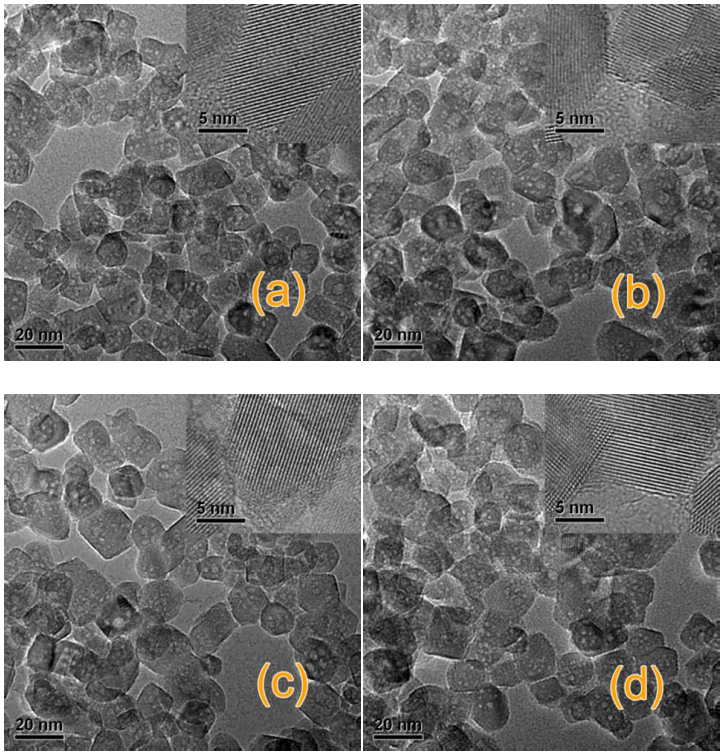

Fig. 2 TEM images of (a) TiO_2, (b) TiO_2-Sn, (c) TiO_2-F, and (d) TiO_2-Sn/F nanoparticles. The inset shows the corresponding HRTEM image of each sample.

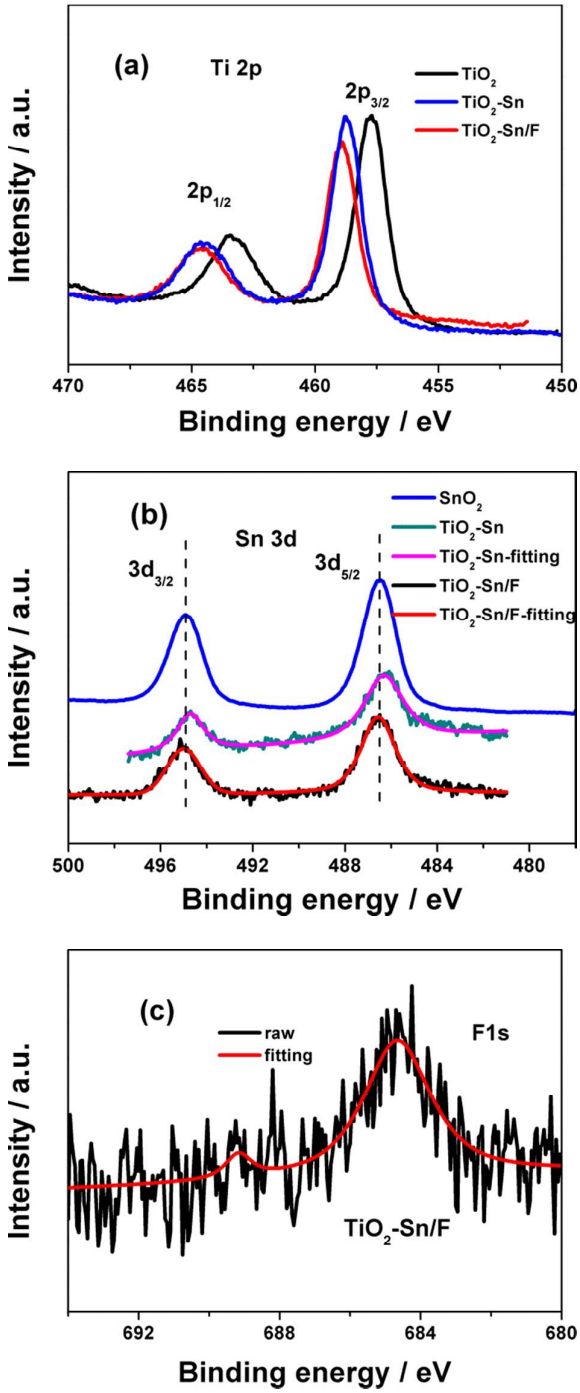

Fig. 3 XPS spectra of Ti_{2p}, Sn_{3d}, and F_{1s} for TiO_2, TiO_2-Sn, and TiO_2-Sn/F samples. SnO_2 was used as a reference here.

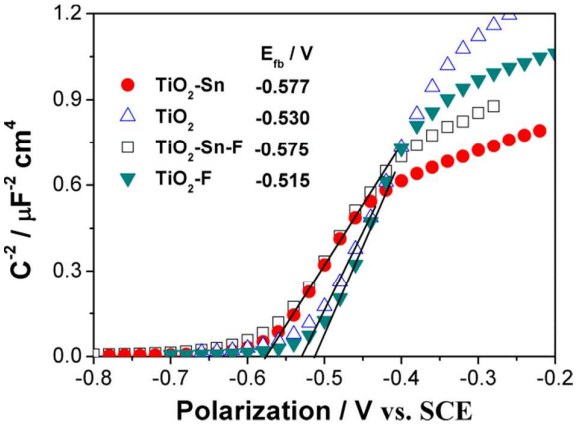

Fig. 4 Mott-Schottky plots for TiO_2 and the doped TiO_2 films.

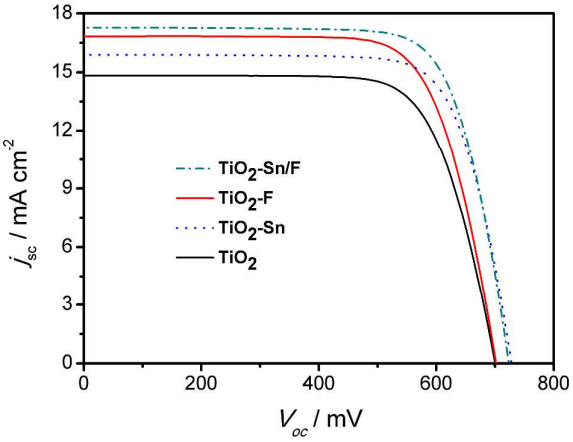

Fig. 5 Photocurrent-voltage characteristics of DSSCs based on TiO_2 and the doped TiO_2 photoanodes under illumination AM1.5. The optimized molar ratios of Sn to Ti in TiO_2-Sn and TiO_2-Sn/F samples (Sn to Ti= 0.5:100) were chosen according to the reference.[37] The optimized molar ratio of F to Ti in TiO_2-Sn/F sample was 0.75:100. TiO_2-F sample (molar ratio, F to Ti= 0.75:100) was chosen as a reference.

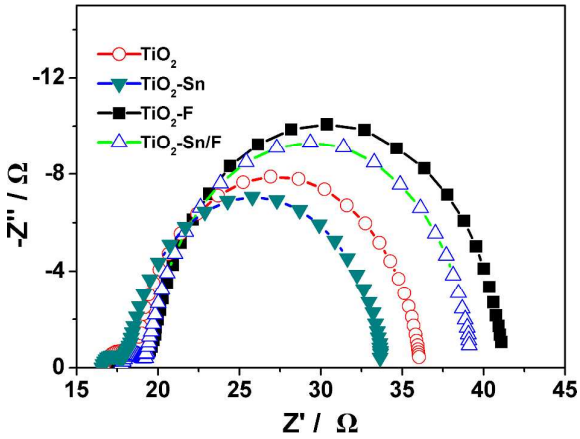

Fig. 6 Nyquist plots from impedance spectra of the four DSSCs based on the equivalent circuit model shown in the Fig. S2.

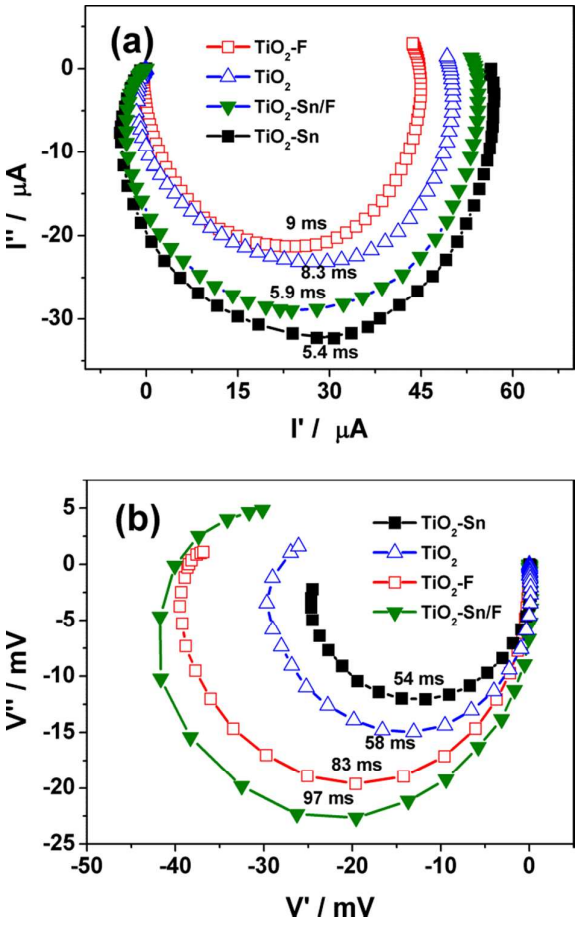

Fig. 7 Complex plane plots of (a) IMPS and (b) IMVS measurements of DSSCs based on TiO_2 and the doped TiO_2.

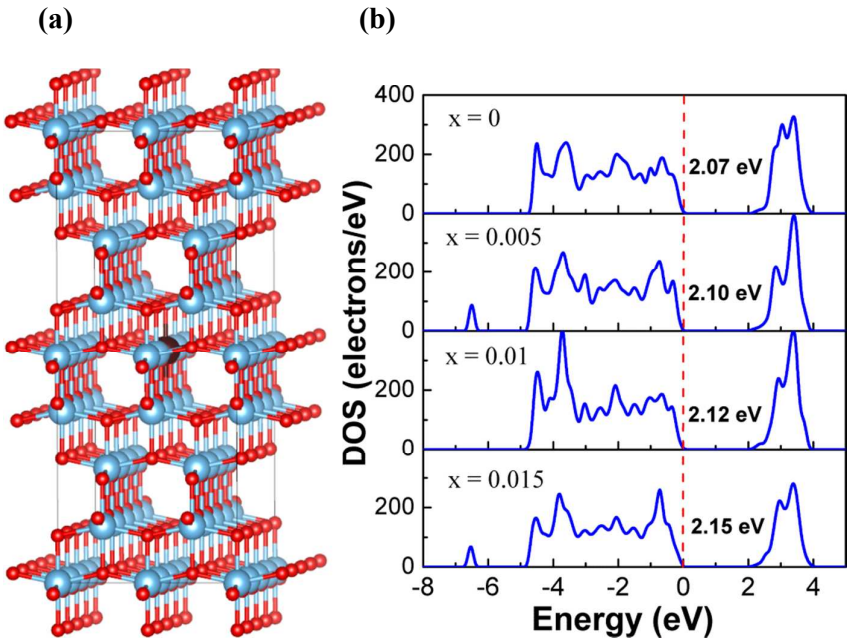

Fig. 8(a) Configurations of $Ti_{0.85}Sn_{0.15}O_2$. Grey-blue ball: Ti; black ball: Sn; red ball: O. (b) Total density of states for $Ti_{1-x}Sn_xO_2$ when x = 0, 0.005, 0.01, and 0.015, respectively. The energy of the valence band maximum of intrinsic TiO_2 is set to 0.

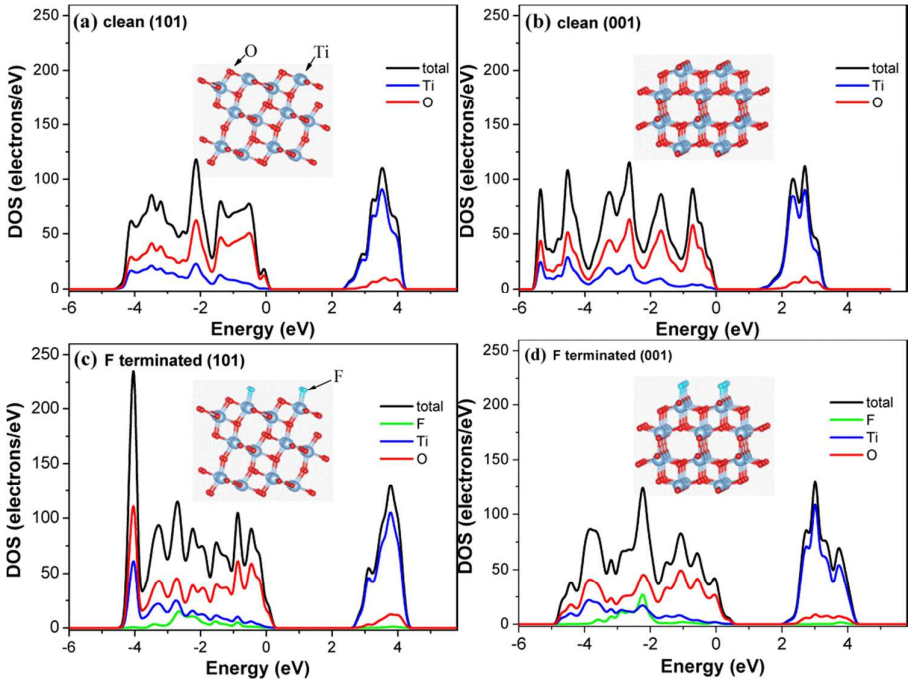

Fig. 9 Calculated total and projected density of states (PDOS) for surfaces of anatase. (a) clean (101); (b) clean (001); (c) F terminated (101); (d) F terminated (001). The insets are the clean surface and F adsorbed surface models for anatase.

Table 1 Comparison of different doping elements for TiO_2 and photovoltaic performance of the DSSCs based on these samples.

Ref.	Doping element	CB shift	Injection efficiency	Transport rate	Electron lifetime	Dye loading	η (%)[a)]
13	W^{6+}			↑	↑	↑	4.14/8.71
14	Zn^{2+}			↑		↑	5.18/5.73
15	Mg^{2+}	positive	↑	↑		→	6.35/7.12
16	V^{5+}			↑	↓	↓	6.01/6.81
17	Ce^{4+}/Ce^{3+}	positive	↑			→	6.4/7.12
9	Sb^{3+}	positive	↑	↑	↓	→	7.36/8.13
18	Ru^{3+}			↑			4.3/5.2
19	Ag+			↓	↑	↑	4.74/6.13
12	Zn^{2+}	negative		↑	↓(1sun)		7.8/8.3
4	Ta^{5+}				↑		4.8/6.7
20	Nb^{5+}		↑		↑	↑	7.4/8.1
21	Eu^{3+}	negative			↑		2.60/3.43
22	Cu^{2+}	negative			↑		5.8/8.1
23	Cr^{3+}	negative			↑		7.1/8.4
24	Zr^{4+}	negative					7.0/8.1
25	Ni	negative		↑	↑	↑	5.2/6.75
26	Li^{+}				↑		1.96/2.60
27	B^{3+}	positive	↑		↑		3.02/3.44
28	S^{6+}	positive	↑	↑			5.56/6.91
29	F-			↑	↑	→	5.62/6.31
30	I^{-}				↑	↑	4.9/7.0
31	N		↑		↓		7.14/8.32
32	Zr^{4+}/N			↑	↑	↑	9.6/12.62
33	N/F^{-}	positive	↑	↑	↑		6.71/8.20
b)	Sn^{4+}	negative		↑	↓	→	7.22/8.14
b)	Sn^{4+}/F^{-}	negative		↑	↑	→	7.22/8.89
b)	Ta^{5+}	positive		↑	↓	→	7.22/8.3
b)	Ta^{5+}/F^{-}	positive		↑	↑	→	7.22/8.78
b)	Nb^{5+}	positive		↑	↓	→	7.22/8.4
b)	Nb^{5+}/F^{-}	positive		↑	↑	→	7.22/9.02
b)	Sb^{3+}	positive	↑	↑	↓	→	7.22/8.36
b)	Sb^{3+}/F^{-}	positive		↑	↑	→	7.22/8.87
b)	F-	positive		↓	↑	→	7.22/8.31

[a)]Photon-to-electron conversion efficiency of DSSCs with pure TiO_2 and the doped TiO_2;
[b)]Data in our work;
[c)]↑, increase; ↓,decrease; →,no change.

Table 2 Lattice parameters, crystalline size and BET surface areas for all the samples

Sample	Lattice parameters		Crystalline size (nm)	Specific surface area ($m^2\ g^{-1}$)
	a (Å)	b (Å)		
TiO_2	3.7808	9.4930	13.8	108.07
TiO_2-Sn	3.7811	9.4978	13.6	110.27
TiO_2-F	3.7807	9.4928	14.1	108.78
TiO_2-Sn/F	3.7812	9.4980	13.6	115.15

Table 3 Photovoltaic characteristics of the DSSCs based on TiO_2 and the doped TiO_2 photoanodes.

Sample	j_{sc} (mA cm^{-2})	V_{oc} (mV)	*FF*	η (%)	Dye loading (×10^{-7} mol cm^{-2})	Film thickness / μm
TiO_2	14.82±0.11	686±7	0.71±0.01	7.22±0.10	1.14±0.04	11.2±0.2
TiO_2-Sn	15.92±0.13	710±5	0.72±0.00	8.14±0.12	1.12±0.05	10.6±0.2
TiO_2-F	16.67±0.09	702±7	0.71±0.01	8.31±0.10	1.16±0.03	11.0±0.2
TiO_2-Sn/F	17.03±0.11	725±8	0.72±0.00	8.89±0.11	1.14±0.04	10.8±0.3

Table 4 Properties determined by electrochemical impedance spectroscopy measurements

Sample	R_k/Ω	R_w/Ω
TiO_2	16.16	1.12
TiO_2-Sn	14.39	0.95
TiO_2-F	20.21	1.24
TiO_2-Sn/F	18.87	0.98

R_w, electron transport resistance.
R_k, charge transfer resistance related to recombination of electrons at theTiO_2/electrolyte interface.

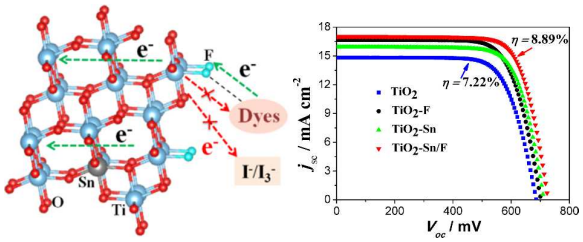

The metal and F dual-doping can synchronously improve electronic transport rate and lifetime for high performance TiO_2-based dye-sensitized solar cells